Challenging Glass Conference Proceedings – Volume 10 – June 2026 – Louter, Bos & Belis (Eds.)
International Conference on the Architectural and Structural Application of Glass
Challenging Glass Conference 10 – 15-17 June 2026 – TU Delft – The Netherlands

Investigation into Out-of-Plane Deformation and Crack Morphology of Laminated Glass at Full Fracture

Dongdong Xie [a, c], Jian Yang [a, c], Xing-er Wang [a, c], Chenjun Zhao [b]

a State Key Laboratory of Ocean Engineering, Shanghai Jiao Tong University, Shanghai 200240, PR China, hxqiay@sjtu.edu.cn
b China Construction Fifth Engineering Bureau the Third Construction (Shenzhen) Co, Ltd, Shenzhen 518131, PR China
c Shanghai Key Laboratory for Digital Maintenance of Buildings and Infrastructure, School of Ocean and Civil Engineering, Shanghai Jiao Tong University, Shanghai 200240, PR China

Abstract

The performance of fully fractured laminated glass (LG) exhibits severe degradation compared with intact and partially fractured ones. This paper investigated two explicit and important outcomes during full fracture of LG, including the out-of-plane deformation and crack morphology. The identification of the initial state of fully fractured LG facilitates its performance evaluation. The fragmentation test was conducted considering three interlayers (ionomer (SG), modified ethylene-vinyl acetate (PVE®), and PVE/polycarbonate/PVE (SGE®)) at three temperatures (20, 50, and 80 ℃). The out-of-plane deformation of partially fractured LG decreases when the remaining intact glass ply fractures. Besides, the fully fractured LG with composite interlayers presents a higher load-bearing capacity than that with single interlayers. The out-of-plane deformation in partially fractured LG leads to denser fragments in the later-fractured glass ply compared with the earlier-fractured glass ply. However, the improving effect weakens/disappears at 80℃, as high temperatures result in degraded interlayer stiffness and interlayer/glass interfaces. Furthermore, the minimum nearest neighbour distance of fragments in the later-fractured glass ply increases compared with that in the earlier-fractured glass ply for most tested cases. This means that the fragments in the later-fractured glass ply are more uniform.

Keywords

Laminated glass, Post-fracture, Crack morphology, Out-of-plane deformation, Composite interlayer

Article Information

- Digital Object Identifier (DOI): 10.47982/cgc.10.662
- Published by Challenging Glass, on behalf of the author(s), at Stichting OpenAccess.
- Published as part of the peer-reviewed Challenging Glass Conference Proceedings, Volume 10, June 2026, 10.47982/cgc.10
- Editors: Christian Louter, Freek Bos & Jan Belis

1. Introduction

Laminated glass (LG), as an important type of safety glass, has drawn much attention in civil engineering, automobile, and aviation. In terms of the pre-fracture performance, researchers have conducted numerous experimental, numerical, and analytical investigations (Belis et al., 2013; Galuppi and Royer-Carfagni, 2012; Jaśkowiec et al., 2017). The Serviceability Limit State and Ultimate Limit State are addressed in CEN/TS 19100-1 (2021) for ensuring the stiffness and load-bearing capacity of pre-fracture glass structures, respectively. In contrast, the evaluation of post-fracture performance mainly focuses on experimental campaigns (Bedon et al., 2026, 2025; Biolzi et al., 2022; Biolzi and Simoncelli, 2022). The favorable tension stiffening (TS) effect from the adhesion of fragments to the interlayer is demonstrated in the post-fracture performance. Limited analytical investigations can be found in Galuppi and Royer-Carfagni (2018) and Bedon et al. (2026), while a numerical exploration was reported by Wang et al. (2021). The non-linear problems in the post-fracture performance evaluation, including the evident fracture-induced out-of-plane deformation (Xie et al., 2026) and contacts between numerous fragments, increase the complexity of the analytical and numerical methods. These non-linearities are mainly dependent on the initial state of specimens in the Post Fracture Limit State (PFLS). Therefore, further investigation needs to be conducted to elucidate the initial state of post-fracture LG.

The fragmentation of tempered glass can trigger the release of center tensile stress and surface compressive stress (Nielsen et al., 2009), which leads to an in-plane expansion effect (Nielsen et al., 2022). However, the in-plane expansion of tempered glass in LG is restricted by the interlayer and remaining glass ply, which is different from monolithic glass (MG). Consequently, the out-of-plane deformation occurs for balancing the cross-sectional bending moments of post-fracture LG. Meanwhile, the crack propagation during the fracture process could be affected by the interlayer and interlayer/glass interfaces. The relationship between surface compressive stress and fragment density for MG is not suitable for the glass plies in LG, especially at relatively low temperatures (Xie et al., 2026). The authors have conducted experimental exploration on LG with one fractured glass ply considering different interlayer types and testing temperatures in Xie et al. (2026). The initial state of the partially fractured LG, including the out-of-plane deformation of LG specimens and crack morphology of the corresponding fractured glass ply, has been determined. It can contribute to the identification of the geometric and contact non-linearities. Note that the identification of the contact non-linearity herein is based on the quantification of the fragment density, rather than the contact properties between fragments.

Furthermore, the mechanical performance of LG would degrade once the remaining intact glass ply in the partially fractured LG is broken. In this case, the overall out-of-plane deformation of fully fractured LG is expected to decrease due to the residual stress release of the second glass ply. Meanwhile, the crack morphology of the later-fractured glass ply could be different from that of the earlier-fractured glass ply, as the out-of-plane deformation of partially fractured LG could introduce additional bending stress into the later-fractured glass ply. Considering that (i) the out-of-plane deformation could exert additional bending moment during in-plane loading and (ii) the fragment size could affect the TS effect, the determination of the initial state of fully fractured LG contributes to a deeper insight into the mechanical behaviors. Moreover, the interlayer type, temperature, and time might affect the initial state of fully fractured LG, as they do for partially fractured LG (Xie et al., 2026). Therefore, the fracture-induced out-of-plane deformation and crack morphologies for fully fractured LG should be investigated to facilitate its performance evaluation and prediction.

This work follows our previous research (Xie et al., 2026), aiming to explore the out-of-plane deformation and crack morphology of fully fractured LG. Fragmentation experiments were conducted, along with crack imaging and fracture-induced out-of-plane deformation measurement. The fracture-induced out-of-plane deformation of LG was investigated during the progressive fracture. The corresponding time dependence was determined by long-term monitoring. Additionally, the crack morphologies between the later- and earlier-fractured glass plies were compared.

2. Fragmentation test

2.1. Specimen

The LG specimens in the fragmentation tests were 1100 mm long and 300 mm wide, consisting of two 8 mm-thick tempered glass layers and one interlayer. Three temperatures (20, 50, and 80℃) were considered in experiments. The measured thickness and surface compressive stress were presented in Table 1. The surface compressive stress was measured using a JF-1E Surface Stress Meter based on the Differential Surface Refractometry (DSR) method. For each glass pane, the stress was measured at five predefined locations (can be seen in Figure 1 of our previous research (Xie et al., 2026)), and the average of the five readings was reported in Table 1. Considering the resolution (1.2 MPa) of the instrument, the surface compressive stress values in Table 1 were rounded to the nearest 1 MPa, while the relative deviation values were reported to one decimal place. The tested specimens were sourced from our previous research (Xie et al., 2026), which featured an initial fractured glass ply. Nearly half of the specimens were adopted in this work. The involved interlayers included SG (SentryGlas® Xtra™), modified EVA (PVE®), and hybrid PVE/polycarbonate (PC)/PVE (SGE®). The nominal thickness of the single interlayer was 1.52 mm. Two composite structures, including 0.76 mm PVE/0.25 mm PC/0.76 mm PVE and 0.76 mm PVE/0.5 mm PC/0.76 mm PVE, were used for SGE. To distinguish the two configurations, SGE-1 and SGE-2 were designated for SGE with 0.25 mm and 0.5 mm thick PC, respectively. The temperature- and time-dependent behaviors of those single/composite interlayers could be found in our previous research (Xie et al., 2024; Yang et al., 2023, 2022). Moreover, the specimen label was designated as the combination of the temperature, interlayer type, and identification number with a connector "_", along with a "D" prefix denoting double glass ply fracture. For instance, the label D_20_SG_1 denoted the first specimen laminated with SG at 20℃.

Table 1: Overall profile of tested LG.

Temperature [°C]	Interlayer	Actual thickness of LG [mm]		Surface compressive stress[a] [MPa]		Surface compressive stress[b] [MPa]		Repli-cate
		Mean	Deviation	Mean	Deviation	Mean	Deviation	
20	SG	17.30	0.13	91	2.4	91	1.8	4
	PVE	16.99	0.03	93	0.6	93	1.0	4
	SGE-1	17.25	0.04	97	1.3	96	0.6	4
	SGE-2	17.47	0.10	94	1.7	95	1.2	4
50	SG	17.42	0.11	93	1.0	93	0.7	3
	PVE	16.83	0.03	95	1.4	96	0.6	3
	SGE-1	17.20	0.03	97	1.7	96	2.4	3
	SGE-2	17.34	0.03	94	1.7	95	0.8	3
80	SG	17.19	0.05	94	0.5	93	1.4	2
	PVE	16.82	0.06	95	1.4	93	2.5	2
	SGE-1	17.10	0.09	91	3.9	92	2.9	2
	SGE-2	17.36	0.06	94	0.2	93	0.8	2

Note: The superscript a represents the glass ply that has been fractured in the previous research. The superscript b denotes the glass ply that is planned to fracture in this work.

2.2. Testing procedure

The developed test chamber mainly included a broad light source, two heat radiation plates, a guiding rail, aluminium frames, PC plates, and a camera, as shown in Fig. 1. The details of the experimental setup could be seen in our previous research (Xie et al., 2026). The setup encompassed the temperature controlling system, out-of-plane deformation scanning system in Fig. 1 (b), and crack morphology capturing system in Fig. 1 (c). The heating function was achieved by two heat radiation plates and a temperature controller. The temperature controller regulated the power supply of the heat radiation plates based on two temperature sensors. The basically consistent readings from the two temperature sensors indicate that the temperature field around the specimen was approximately uniform, assisted by the forced air convection generated by the two fans inside the chamber. Due to the lack of a cooling function in the developed chamber, the air conditioner in the room was used to control the test temperature of 20°C. The partially fractured LG specimen was installed vertically with four-point support, as illustrated in Fig. 2 (a). Additionally, four pairs of restrictors were used to constrain the four corners of the specimens. The reserved space between the specimen and the restrictors allowed the specimen to expand in the in-plane and out-of-plane directions. The specimens were subjected to heat soaking in the test chamber for at least 12 hours to ensure they reached the target temperature.

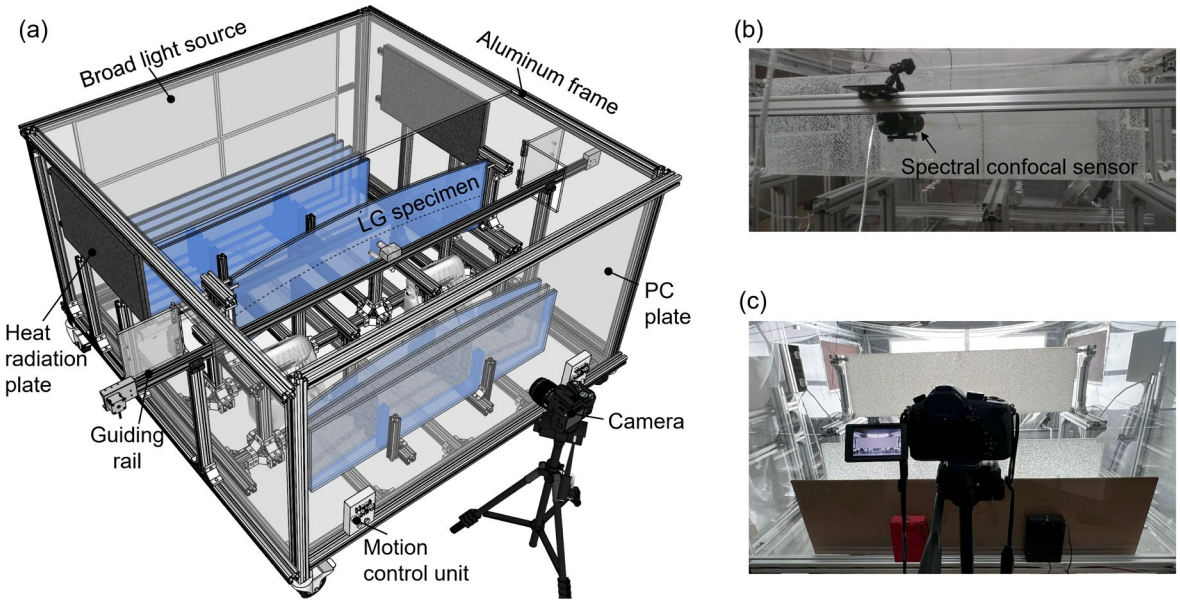

Fig. 1: Experimental setup. (a) Overall schematic. (b) Physical diagram for out-of-plane deformation measuring. (c) Physical diagram for crack morphology capturing.

After installing the partially fractured LG specimen in Fig. 2 (a), the main experimental steps are as follows: (i) The out-of-plane deformation of the specimen was scanned along the center line using a spectral confocal sensor, as shown in Fig. 2 (b). (ii) The fracture of the intact glass ply in partially fractured LG was introduced by gradually impacting a point located 13 mm from the center of the long edge according to EN 12150-1 (2015). The impact point is marked by the red cross and indicated by the arrow in Fig. 2 (a). (iii) The out-of-plane deformation of fully fractured LG was scanned 5 minutes after fracture, as illustrated in Fig. 2 (c). Besides, the out-of-plane deformation 10, 20, 30, and 30+ minutes after fracture for some specimens were measured. The timestamps selected were consistent with our previous research (Wang et al., 2024; Xie et al., 2026). The measurement 30+ minutes after fracture means that the specimen underwent manual shaking in the out-of-plane direction. (iv) The crack morphology was captured by a camera approximately 40 minutes after fracture (Fig. 2 (d)), which was achieved based on an adhered polyvinyl chloride (PVC) plate with 0.3 mm thickness. The physical cracks of the fractured glass ply facing the camera were projected on the PVC plate when the broad light source was turned on.

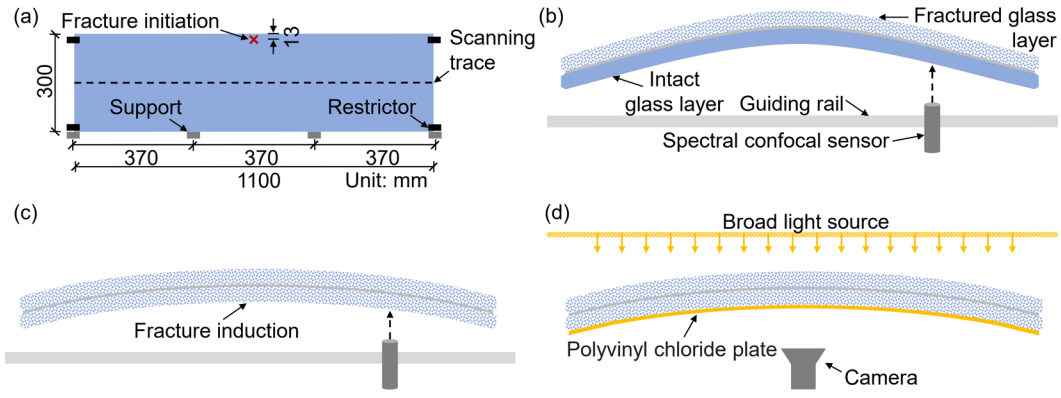

Fig. 2: Testing procedure. (a) Initial state (front view). (b) First step (top view). (c) Second and third steps (top view). (d) Fourth step (top view).

Although the specimens with two fractured glass plies in this work are more complicated than the partially fractured LG, the crack morphology capturing system in Xie et al. (2026) is effective and can be adopted in this work. The mechanism of crack capturing in fully fractured LG is shown in Fig. 3. The light reflection and refraction at the interfaces between the interlayer and glass are neglected due to the relatively close refractive indices of these two materials (Nur-E-Alam et al., 2024). The physical crack presents the contracted central zone and expanded surfaces due to the release of center tensile stress and surface compressive stress (Nielsen et al., 2009). When parallel light is normally incident on tempered laminated glass, a significant amount of reflection and refraction occurs at the fractured surfaces, thereby resulting in a reduction in light intensity after transmission through the physical cracks. Consequently, an evident black region appears on the PVC plate, corresponding to the physical crack from Layer B glass in Fig. 3. In comparison, the light intensity at the projected regions of cracks from Layer A glass is supplemented by extensive reflected and refracted light. Therefore, the projected cracks from the Layer A glass exhibit blurred shadows, as shown in Fig. 3. The significant difference in the projected features of cracks between the two glass plies contributes to the crack identification in the Layer B glass (the target glass ply in this work). Moreover, the diffuse reflection in the fractured regions, where numerous glass particles have irregular surfaces (Sheikh et al., 2021), could increase the light intensity in the projected crack-region of the Layer A glass, further improving the contrast of projected crack-region intensity between the Layer A and B glasses. In addition, to ensure the effectiveness of the planar light source in approximating collimated illumination and to achieve a clear distinction between the crack projections from the Layers A and B, the distance between the planar light source and the projection screen should not be excessively large. In this experiment, this distance was set to 920 mm.

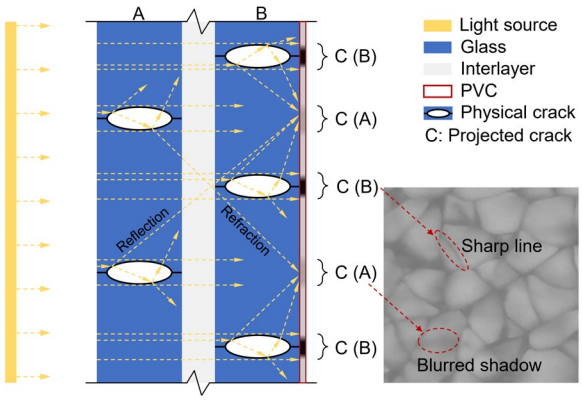

Fig. 3: Mechanism of crack imaging in fully fractured LG.

3. Data processing

3.1. Out-of-plane deformation measurement

Due to the rail-to-specimen non-parallelism caused by the specimen installation, the corresponding correction is addressed in Fig. 4. The coordinate system transformation from *X*-*Y* (the measurement coordinate system) to *P*-*Q* (the correction coordinate system) follows Eqs. (2)-(5). The coordinates of the right and left endpoints of a specimen are written as $(0, y_1)$ and (x_2, y_2) in the *X*-*Y* coordinate system, respectively. Based on the relative magnitude between y_1 and y_2, the mathematical deduction falls into two categories. Moreover, the imperfection of the guiding rail $u_r(p)$ is used to compensate for the deformation data $u_{c,1}(p)$ to accurately obtain the realistic out-of-plane deformation $u_{c,2}(p)$ based on Eq.

(6). The mirrored measurement (Belis et al., 2011) and corresponding results of the rail imperfection can be found in Xie et al. (2026).

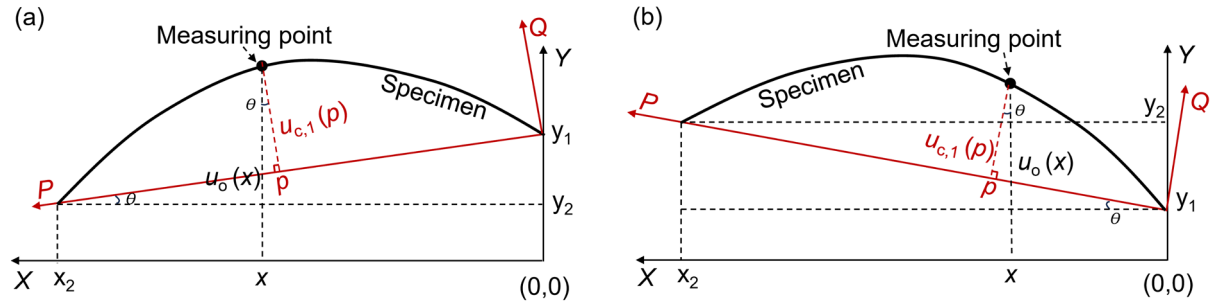

Fig. 4: Coordinate definition and non-parallelism correction. (a) Case 1 ($y_1 \geq y_2$). (b) Case 2 ($y_1 < y_2$).

$$\theta = \arctan\left(|y_1 - y_2|/x_2\right) \tag{1}$$

$$p = x/\cos\theta - [u_o(x) - y_2 - (x_2 - x)\tan\theta]\sin\theta \tag{2}$$

Case 1 ($y1 \geq y2$)

$$u_{c,1}(p) = [u_o(x) - y_2 - (x_2 - x)\tan\theta]\cos\theta \tag{3}$$

$$p = x/\cos\theta + [u_o(x) - y_1 - x\tan\theta]\sin\theta \tag{4}$$

Case 2 ($y1 < y2$)

$$u_{c,1}(p) = [u_o(x) - y_1 - x\tan\theta]\cos\theta \tag{5}$$

$$u_{c,2}(p) = u_{c,1}(p) + u_r(p) \tag{6}$$

Where the coordinates (x, $u_o(x)$) and (p, $u_{c,1}(p)$) represent the measuring point in the X-Y and P-Q coordinate systems in Fig. 4, respectively. θ denotes the included angle between the two coordinate systems.

3.2. Crack morphology identification

The crack identification method in fully fractured LG is the same as that in partially fractured LG in Xie et al. (2026). The crack morphology of the Layer A glass has been captured in our previous work (Xie et al., 2026), and the corresponding blurred shadows present a slight/negligible influence on the crack projection of the Layer B glass, as shown in Fig. 3. Therefore, the extant image processing is still effective to identify the crack morphology of the Layer B glass, which includes (i) the original image is corrected for distortion, (ii) the Trainable Weka Segmentation plugin (Arganda-Carreras et al., 2017) in ImageJ software is used to identify cracks, (iii) the binarization and distance transformation algorithms are applied to extract the crack skeleton, (iv) the skeleton is manually inspected, along with tracing some faint cracks, (v) the fragments are segmented based on the MorphoLibJ plugin (Legland et al., 2016). The fragment statistics for the Layer B glass are conducted over 10 distinct 50×50 mm^2 sub-regions, each highlighted in blue on Fig. 5. The blue sub-regions in the Layer B glass occupy the same relative positions within each ply as the red regions do in the Layer A glass. The position consistency

of the statistical regions between the Layer A and B glasses contributes to the effective comparison of the fragment number. The statistical principle of fragment number refers to EN 12150-1 (2015).

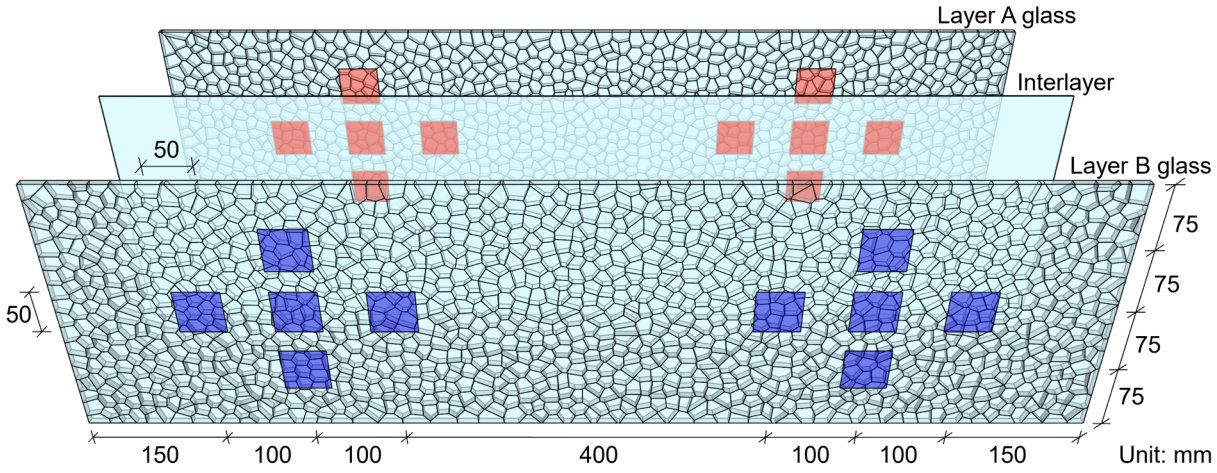

Fig. 5: Regions for fragment statistic.

4. Results and discussion

4.1. Out-of-plane deformation

The fracture-induced out-of-plane deformations for partially and fully fractured LG are presented in Fig. 6. It is clear from Fig. 6 (a) that the out-of-plane deformation exhibits an evident decrease in magnitude once the Layer B glass fractures. Besides, the roller wave distortion could be found in the deformation curves of partially and fully fractured LG in Fig. 6 (a). This is attributed to the horizontal tempering of specimens. Therefore, the adjacent-averaging method is used to smooth the data. The maximum value of the smoothed curve is taken as the characteristic out-of-plane deformation u_{max} induced by glass fracture. The maximum out-of-plane deformations of specimens at different temperatures are displayed in Fig. 6 (b). In addition, the corresponding reduced amplitude of u_{max} due to fracture of the Layer B glass is included.

In general, increasing temperature could make the out-of-plane deformation of partially fractured LG less evident due to the decreased interlayer stiffness and interfacial performance at high temperatures (Xie et al., 2026). However, the temperature affects the out-of-plane deformation of fully fractured LG, which does not show an evident monotonic relationship when compared with that of partially fractured LG in Fig. 6 (b). The out-of-plane deformation of fully fractured LG increases across the four series when the temperature rises from 20℃ to 50℃. This might result from the relatively lower additional stress in the intact glass ply caused by the out-of-plane bending deformation of partially fractured LG at 50℃. Accordingly, there is less in-plane expansion tendency in the intact glass at 50℃ when its stress releases, leading to a smaller reduced out-of-plane deformation u_d compared with that at 20℃, as shown in Fig. 6 (b).

At 80℃, the out-of-plane deformation of fully fractured LG presents more variability than that at 20℃ and 50℃. This is mainly attributed to the low stiffness of SG and PVE at 80℃. The fully fractured LG retains some structural integrity through the interlayer and interlayer/glass interfaces. Consequently, the load-bearing capacity of fully fractured LG is relatively low at 80℃, which results in higher sensitivity to the external force magnitude. In this case, the fracture manner of the Layer B glass

(manual gradual impact) introduces variability in the out-of-plane deformation of fully fractured LG. Moreover, the impact by a hammer leads to higher out-of-plane deformation for fully fractured PVE LG compared with that for partially fractured one at 80℃. Furthermore, the fully fractured SG LG at 80℃ exhibits out-of-plane deformations in the opposite direction to the partially fractured SG LG, which might result from the relatively small out-of-plane deformation of the partially fractured specimen. Accordingly, the fully fractured specimen is more prone to out-of-plane expansion toward the side of the Layer B glass.

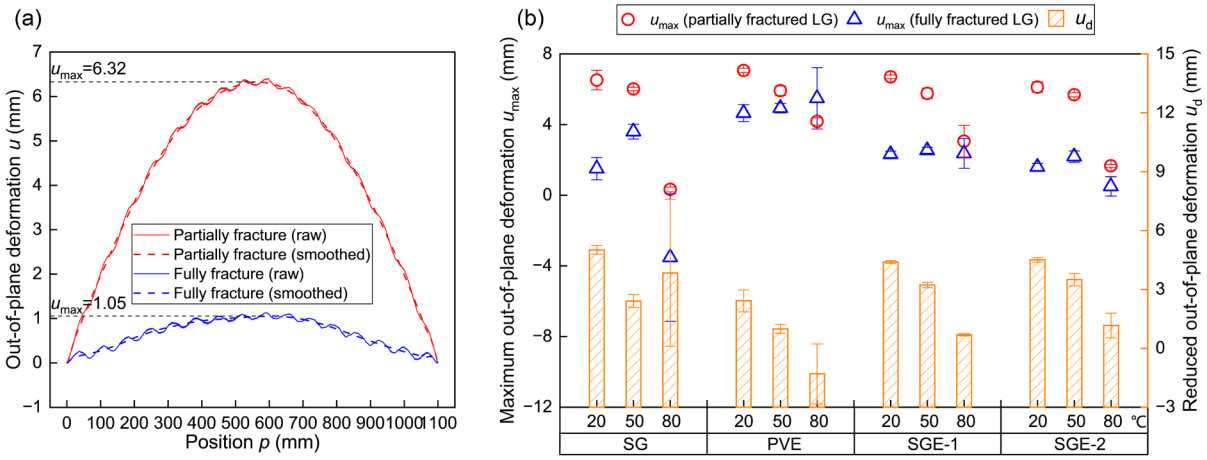

Fig. 6: Fracture-induced out-of-plane deformations for partially and fully fractured LG. (a) Characteristic deformation curves (Specimen D_20_SG_1). (b) Maximum deformations and corresponding reduction at different temperatures. The out-of-plane deformation of fully fractured LG is measured 5 minutes after fracture of the Layer B glass.

The representative results for the change of out-of-plane deformation over time are shown in Fig. 7. Basically, the deformation decreases with increasing time due to the relaxation characteristic of the polymeric interlayer (Xie et al., 2024). However, the stiffness of SG and PVE is relatively low at 50℃ and 80℃, which makes the fully fractured LG more sensitive to the mechanical vibration during the movement of the spectral confocal sensor. Accordingly, the out-of-plane deformation for SG series at 50℃ and PVE series at 80℃ presents fluctuations over time in Fig. 7 (a). Moreover, the results in Fig. 7 (b) reveal that the out-of-plane deformation of fully fractured LG could reduce under the disturbance of external forces. Increasing temperature enhances the reduced amplitude due to the low stiffness of the interlayer at high temperatures. Furthermore, it can be seen from Fig. 6 (b) and Fig. 7 (a) that the out-of-plane deformation of fully fractured LG presents a decreasing tendency when the thickness of PC layer increases among PVE, SGE-1, and SGE-2 series. The relatively stiff PC could restrict the out-of-plane expansion, which also contributes to a high post-fracture stiffness of SGE LG. Therefore, the reduced deformation caused by manual shaking for SGE-1 and SGE-2 series is evidently smaller than that for SG and PVE series at 20, 50 and 80℃, as shown in Fig. 7 (b).

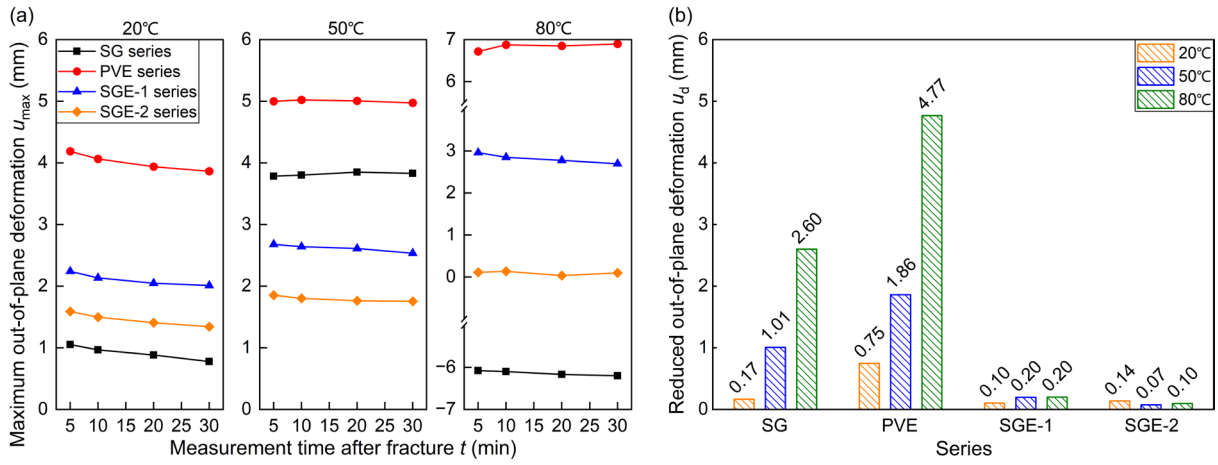

Fig. 7: Changes of out-of-plane deformation for fully fractured LG in the range of (a) 5 – 30 minutes, and (b) 30 – 30+ minutes after fracture of the Layer B glass in LG. The reduced out-of-plane deformation in (b) results from manual shaking.

4.2. Crack morphology

The key crack morphology includes fracture feature, fragment number N_{50} and the minimum nearest neighbor distance η_{min}. The latter two indices can be used to reconstruct the fractured glass based on Voronoi tessellation (Zhu et al., 2023). Considering that the crack morphology of the Layer A glass has been discussed in detail by Xie et al. (2026), this section mainly presents the cracks in the Layer B and corresponding comparison between the two glass plies.

4.3. Fracture feature

The captured cracks in the Layer B glass are presented in Fig. 8 (c) and (d), while Fig. 8 (a) and (b) exhibit cracks in the Layer A glass. It is clear from Fig. 8 (a) and (c) from that the fragment patterns in the entire specimen can be roughly divided into four regions, which include a triangular impact-influenced region beneath the impact point (Region 2), an edge-influenced region around the perimeter (Region 3), and interior regions unaffected by impact and edges (Regions 1 and 4). Affected by the impact, the Region 2 presents radial cracks with a higher density than those in the Regions 1 and 4. Besides, the cracks in the Region 3 are influenced by the complicated stress distribution and stress wave reflection at the edges. In comparison, the Regions 1 and 4 can be recognized as free of the effect of the impact and edges. Therefore, the ten regions for fragment statistic in Fig. 5 are chosen within the Regions 1 and 4. Moreover, two whirl-fragments near the fracture initiation point in the Layer B glass can be seen in Fig. 8 (d), which is similar to those in the Layer A glass in Fig. 8 (b).

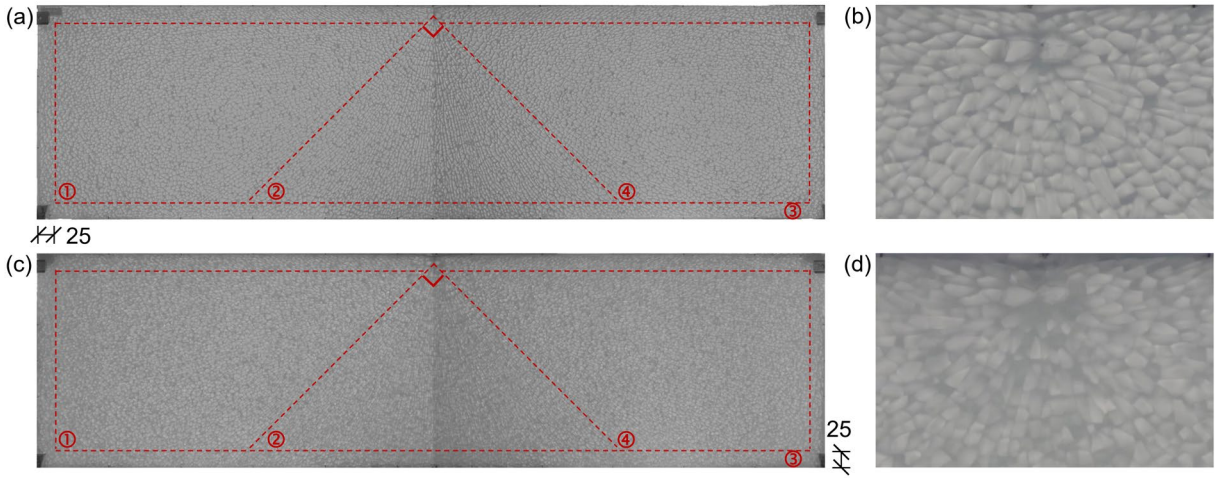

Fig. 8 Fracture feature of the two glass plies in LG (Specimen D_20_PVE_1). (a) and (b) are fragment patterns across the entire specimen and near the fracture initiation point for the Layer A glass, respectively. (c) and (d) represent fragment patterns across the entire specimen and near the fracture initiation point for the Layer B glass, respectively. Given the relatively large size of the specimen, the cracks across the entire specimen were photographed in two separate sessions, covering the left and right parts, respectively. Consequently, there is a discontinuity in light intensity at the stitching position of the left and right crack images in (a) and (c). Units are in millimeters.

4.4. Fragment number N_{50}

Based on the crack identification method in Section 3.2, the fragment number N_{50} can be counted. The average N_{50} across the ten regions in Fig. 5 is taken as the representative N_{50} of the glass ply, which is presented in Fig. 9. As shown in Fig. 9, N_{50} for the Layer B glass is higher than that for the Layer A glass in LG at 20℃ and 50℃. The improvement rate decreases with increasing temperature. The fragment density increases by 68.56% for SG series at 20℃. The additional bending stress in the intact glass ply due to the out-of-plane deformation of the partially fractured LG contributes to the increase in fragment density in the Layer B glass. Moreover, the Layer B glass for SG and PVE series presents a reduced N_{50} compared with that of the Layer A glass at 80℃. However, the stiff PC layer for SGE-1 and SGE-2 series might affect the interaction between the stress wave and crack propagation in the fragmentation process of the Layer B glass. Consequently, the fragment density of the Layer B glass is slightly higher than that of the Layer A glass for SGE-1 and SGE-2 series at 80℃, as illustrated in Fig. 9. Nonetheless, it is reasonable to assume a consistent fragment density between the two glass plies in LG at 80℃ considering the relatively high data fluctuation (Fig. 9) and low stiffness of SG and PVE at high temperatures. Furthermore, it should be noted that the denser fragments in the Layer B glass did not cause the direction of the out-of-plane deformation of fully fractured LG to reverse (i.e., shift toward the Layer B glass). as shown in Fig. 6 (b), most fully fractured LG presents the out-of-plane deformation oriented toward the Layer A glass. This phenomenon may be attributed to the interlocking effect between fragments in the Layer A glass, which provides a mechanical resistance against deformation reversal. Given that the out-of-plane deformation is sensitive to external force (as demonstrated in Fig. 7 (b)), the fracture initiation manner also might contribute to maintaining direction when the intact glass in partially fractured LG undergoes subsequent breakage.

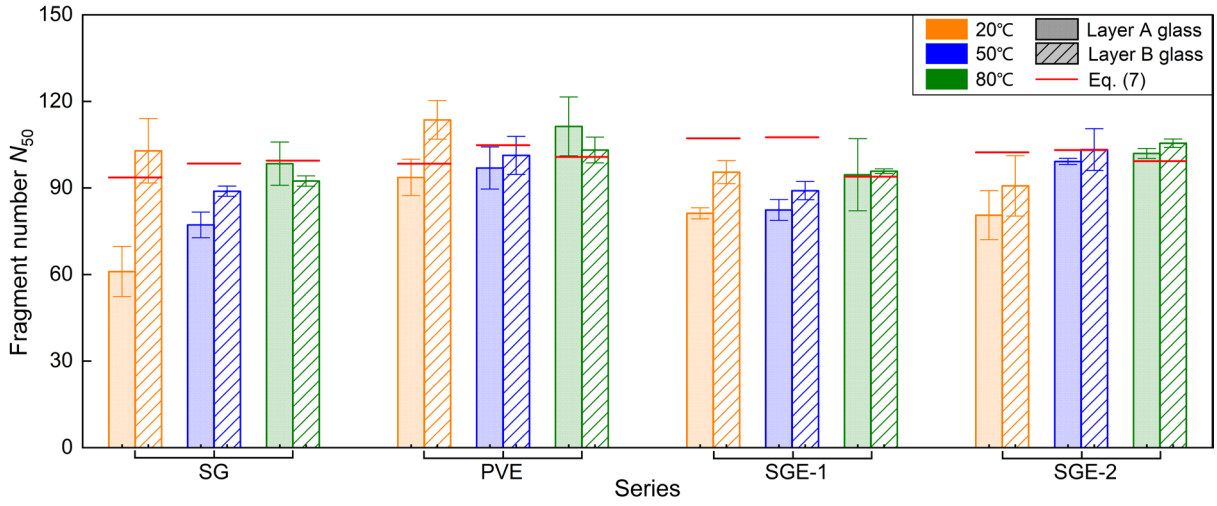

Fig. 9: Fragment number N_{50} of the two glass plies in LG.

$$N_{50} = 2.6556 \times \sigma_s - 148.89 \quad (7)$$

Weis and Siebert (2022) analysed the fragment number N_{50} for glass laminates with PVB (Trosifol® Clear/Ultra Clear and Trosifol® Extra Stiff) and SG at 20℃. Their results reveal that, for PVB (Trosifol® Extra Stiff) and SG LG, the N_{50} value of the Layer B increases by 42.86% and 23.00% compared with the Layer A, respectively. In contrast, the increase in N_{50} is negligible for PVB (Trosifol® Clear/Ultra Clear), resulting from its low elastic modulus. Moreover, the increase rate of 23.00% in Weis and Siebert (2022) is substantially lower than that in this work (68.56% for SG series at 20℃). It could be attributed to the higher surface compressive stress (110 MPa) of the specimens used by Weis and Siebert (2022). The resulting high baseline value (N_{50} = 100 for the Layer A) in Weis and Siebert (2022) leads to a relatively smaller percentage increase in N_{50}.

Pourmoghaddam and Schneider (2018) conducted numerous fragmentation tests and established a linear relationship between surface compressive stress σ_s and fragment number N_{50} for MG with different thicknesses. The correlation for 8 mm thick MG is presented in Eq. (7), which is taken as the benchmark. Considering the close surface compressive stresses of the two glass plies in LG (Table 1), the average σ_s is used to calculate N_{50} by Eq. (7), as shown in Fig. 9. In terms of the comparison of fragment density between the Layer A glass in LG and MG, the potential reason that the interlayer decreases the fragment density is the reduction of the center tensile stress by restricting the in-plane expansion of the fractured glass ply during the fracture process (Xie et al., 2026). However, the initial in-plane and out-of-plane deformations of the partially fractured LG increase the complexity of the center tensile stress in the Layer B glass further, resulting in a varying relative quantity of N_{50} between the Layer B glass and MG. Specifically, the Layer B glass for SG and PVE series at 20℃ present a higher N_{50} than MG, whilst the remaining cases at 20℃ and 50℃ exhibit an opposite tendency. By comparing N_{50} at 20℃ across the four series in Fig. 9 and the corresponding out-of-plane deformation in Fig. 6 (b), it can be concluded that the interlayer or interlayer/glass interfaces also affect N_{50} of the Layer B glass. The influential mechanism could be investigated in depth by refined numerical simulations in future work. Moreover, N_{50} of the Layer B glass at 80℃ is basically close to that of MG (Eq. (7)), as shown in Fig. 9. The relatively large deviation for SG and SGE-2 series might result from fragment identification,

where the dense fragments at 80°C decrease the contrast of projected cracks between the two glass plies in Fig. 3.

4.5. Minimum nearest neighbor distance η_{min}

The nearest neighbor distance η means the minimum centroid distance between a target fragment and its adjacent fragments. In this case, η_{min} can be obtained by analyzing η of each fragment within the target region. It should be noted that the fragments at the edges of the region are excluded for the statistic of η due to their incompleteness. Besides, η_{min} of all tested specimens in Xie et al. (2026) is supplemented in this section considering that the previous research lacks its report, which is exhibited in Fig. 10 (a). Meanwhile, η_{min} of the Layer A and B glasses of tested specimens in this work is presented in Fig. 10 (b). Fig. 10 (a) shows that increasing temperature can decrease η_{min} for the four series. It is reasonable considering that the fragment size decreases with a rise in temperature (Xie et al., 2026). Besides, the relationship between fragment size and η_{min} for the Layer B glass is similar to that for the Layer A glass. For instance, the Layer B glass at 20°C presents the minimum N_{50} among the three temperatures for SG series (Fig. 9), corresponding to the maximum η_{min} at 20°C (Fig. 10 (b)).

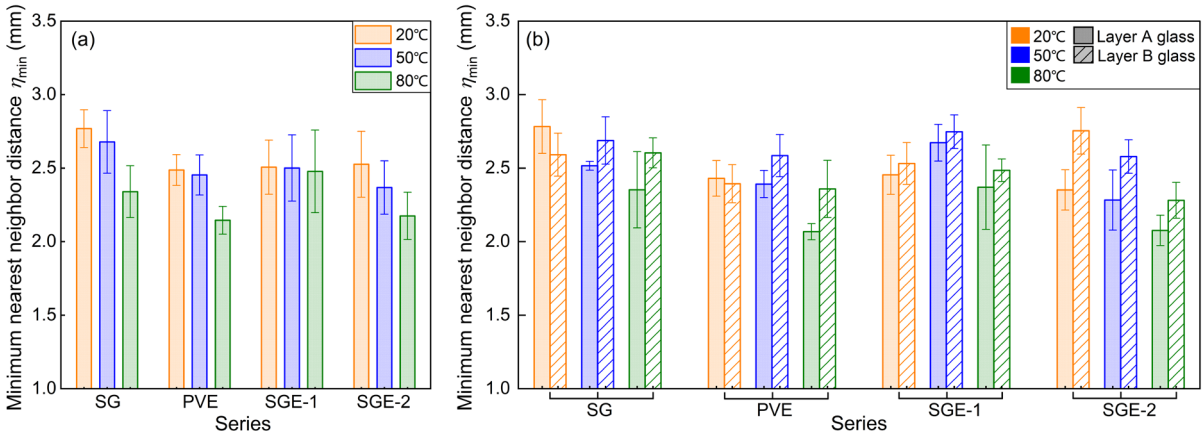

Fig. 10: Minimum nearest neighbor distance η_{min} of tested specimens (a) in Xie et al. (2025), and (b) in this work.

Fig. 10 (b) shows that η_{min} of the Layer B glass is higher than that of the Layer A glass for most cases. This means that the fragments in the later-fractured glass ply exhibit greater uniformity compared to those in the earlier-fractured glass ply. However, the Layer B glass for SG and PVE series at 20°C presents a lower η_{min} than the Layer A glass. It might be attributed to the evident enhancement of N_{50} between the two glass plies for SG and PVE series at 20°C compared with the remaining cases, as shown in Fig. 9. In this case, the influence of the decrease in fragment size is higher than that of random fluctuation from fragment non-uniformity. Furthermore, it should be noted that the fluctuation range of η_{min} (2.0 – 3.0 mm) is relatively small across all tested specimens, which might have a slight/negligible influence on the mechanical properties of post-fracture LG. The numerical reconstruction based on Voronoi tessellation contributes to analyzing the influence of measured η_{min} in future work.

5. Conclusion

This paper experimentally explored the fracture-induced out-of-plane deformation for fully fractured laminated glass (LG) and corresponding crack morphologies in the two glass plies. Three temperatures and four interlayers were considered. The results indicate that the out-of-plane deformation of fully fractured LG presents an evident decrease compared with partially fractured one, especially at relatively low temperatures. Besides, the fully fractured LG with composite interlayers exhibits a higher stiffness than that with single interlayers. The addition of polycarbonate ply in composite interlayers could contribute to the increase in load-bearing capacity in the Post Fracture Limit State (PFLS). Moreover, the later-fractured glass ply shows denser fragments compared with the earlier-fractured glass ply in LG at 20℃ and 50℃, which might result from the additional bending stress in the later-fractured glass ply caused by out-of-plane deformation of partially fractured LG. Furthermore, the fragment uniformity for the later-fractured glass ply improves in comparison with the earlier-fractured glass ply. The investigations on the out-of-plane deformation and crack morphology of fully fractured LG contribute to a deeper insight into the mechanical behaviors of LG in the PFLS.

Acknowledgements

This study was funded by the Key R&D Program of Shandong Province, China [Grant No. 2024TSGC0467, 2024TSGC002] and National Natural Science Foundation of China [Grant No. 52578299]. The authors thank the Henan Zhongbo Glass Co., Ltd. for supplying testing materials.

References

Arganda-Carreras, I., Kaynig, V., Rueden, C., Eliceiri, K.W., Schindelin, J., Cardona, A., Sebastian Seung, H., 2017. Trainable weka segmentation: a machine learning tool for microscopy pixel classification. Bioinformatics 33, 2424–2426. https://doi.org/10.1093/bioinformatics/btx180

Bedon, C., Del Bello, R., Cella, N., Cozzarini, L., Fasan, M., 2026. Residual mechanical capacity of small-scale partially fractured annealed laminated glass elements subjected to a quasi-static cyclic protocol. Engineering Failure Analysis 186, 110462. https://doi.org/10.1016/j.engfailanal.2025.110462

Bedon, C., Kozłowski, M., Cella, N., 2025. Gaps in the post-breakage out-of-plane bending stiffness assessment of 2-ply partially damaged laminated glass elements under short-term quasi-static loads. Engineering Structures 327, 119617. https://doi.org/10.1016/j.engstruct.2025.119617

Belis, J., Bedon, C., Louter, C., Amadio, C., Van Impe, R., 2013. Experimental and analytical assessment of lateral torsional buckling of laminated glass beams. Engineering Structures 51, 295–305. https://doi.org/10.1016/j.engstruct.2013.02.002

Belis, J., Mocibob, D., Luible, A., Vandebroek, M., 2011. On the size and shape of initial out-of-plane curvatures in structural glass components. Construction and Building Materials 25, 2700–2712. https://doi.org/10.1016/j.conbuildmat.2010.12.021

Biolzi, L., Cattaneo, S., Simoncelli, M., 2022. Post-failure behavior of 2-ply laminated glass plates with different interlayers. Engineering Fracture Mechanics 268, 108496. https://doi.org/10.1016/j.engfracmech.2022.108496

Biolzi, L., Simoncelli, M., 2022. Overall response of 2-ply laminated glass plates under out-of-plane loading. Engineering Structures 256, 113967. https://doi.org/10.1016/j.engstruct.2022.113967

CEN/TS 19100-1, 2021. Design of glass structures - part 1: basis of design and materials. Comite Europeen de Normalisation.

EN 12150-1, 2015. Glass in building – thermally toughened soda lime silicate safety glass – part 1: definition and description. Comite Europeen de Normalisation.

Galuppi, L., Royer-Carfagni, G., 2018. The post-breakage response of laminated heat-treated glass under in plane and out of plane loading. Composites Part B: Engineering 147, 227–239. https://doi.org/10.1016/j.compositesb.2018.04.005

Galuppi, L., Royer-Carfagni, G.F., 2012. Effective thickness of laminated glass beams: new expression via a variational approach. Engineering Structures 38, 53–67. https://doi.org/10.1016/j.engstruct.2011.12.039

Jaśkowiec, J., Pluciński, P., Stankiewicz, A., Cichoń, Cz., 2017. Three-dimensional modelling of laminated glass bending on two-dimensional in-plane mesh. Composites Part B: Engineering 120, 63–82. https://doi.org/10.1016/j.compositesb.2017.03.008

Legland, D., Arganda-Carreras, I., Andrey, P., 2016. MorphoLibJ: integrated library and plugins for mathematical morphology with ImageJ. Bioinformatics 32, 3532–3534. https://doi.org/10.1093/bioinformatics/btw413

Nielsen, J.H., Olesen, J.F., Stang, H., 2009. The fracture process of tempered soda-lime-silica glass. Experimental Mechanics 49, 855–870. https://doi.org/10.1007/s11340-008-9200-y

Nielsen, J.H., Schneider, J., Kraus, M.A., 2022. The in-plane expansion of fractured thermally pre-stressed glass panes - an equivalent temperature difference model for engineering glass design. Construction and Building Materials 327, 126849. https://doi.org/10.1016/j.conbuildmat.2022.126849

Nur-E-Alam, M., Vasiliev, M., Yap, B.K., Islam, M.A., Fouad, Y., Kiong, T.S., 2024. Design, fabrication, and physical properties analysis of laminated low-E coated glass for retrofit window solutions. Energy and Buildings 318, 114427. https://doi.org/10.1016/j.enbuild.2024.114427

Pourmoghaddam, N., Schneider, J., 2018. Experimental investigation into the fragment size of tempered glass. Glass Structures & Engineering 3, 167–181. https://doi.org/10.1007/s40940-018-0062-0

Sheikh, M.Z., Atif, M., Li, Y., Zhou, F., Raza, M.A., Dar, U.A., Gao, G., Wang, Y., 2021. Damage mechanisms and energy absorption of aluminosilicate glass under compression/tensile loading. Construction and Building Materials 288, 123088. https://doi.org/10.1016/j.conbuildmat.2021.123088

Wang, X., Yang, J., Pan, Z., Wang, F., Meng, Y., Zhu, Y., 2021. Exploratory investigation into the post-fracture model of laminated tempered glass using combined voronoi-FDEM approach. International Journal of Mechanical Sciences 190, 105989. https://doi.org/10.1016/j.ijmecsci.2020.105989

Wang, Y., Wang, X.-E., Yang, J., Xie, D., Pang, K., Pan, Z., 2024. Experimental investigation into the expansion behaviour of thermally tempered laminated glass plates at asymmetric fracture. Construction and Building Materials 442, 137586. https://doi.org/10.1016/j.conbuildmat.2024.137586

Weis, J., Siebert, G., 2022. Einfluss der zwischenschicht auf das bruchverhalten von verbundsicherheitsglas. ce papers 5, 241–253. https://doi.org/10.1002/cepa.1672

Xie, D., Yang, J., Wang, X.-E., Wang, Y., Pan, Z., Zhao, C., 2026. Temperature and time dependences of fragment generation and out-of-plane deformation in fractured tempered glass laminates. Thin-Walled Structures 218, 113959. https://doi.org/10.1016/j.tws.2025.113959

Xie, D., Yang, J., Zhao, C., Wang, X., 2024. Comprehensive investigation into the thermal rheological behavior and relaxation characteristic of single/composite polymers in laminated glass. Thin-Walled Structures 195, 111369. https://doi.org/10.1016/j.tws.2023.111369

Yang, J., Wang, Y., Wang, X., Hou, X., Zhao, C., Ye, J., 2022. Local bridging effect of fractured laminated glass with EVA based hybrid interlayers under weathering actions. Construction and Building Materials 314, 125595. https://doi.org/10.1016/j.conbuildmat.2021.125595

Yang, J., Zhao, C., Zhang, Y., Wang, X., Wang, Y., Xie, D., 2023. Constitutive models for temperature-, strain rate- and time-dependent behaviors of ionomers in laminated glass. Journal of Materials Science 58, 3608–3624. https://doi.org/10.1007/s10853-023-08222-y

Zhu, Y., Yang, J., Wang, X., Xie, D., Hou, X., 2023. Morphological characterization and reconstruction of fractured heat-treated glass. Journal of Non-Crystalline Solids 616, 122455. https://doi.org/10.1016/j.jnoncrysol.2023.122455

Challenging Glass Conference Proceedings – Volume 10 – June 2026 – Louter, Bos & Belis (Eds.)
International Conference on the Architectural and Structural Application of Glass
Challenging Glass Conference 10 – 15-17 June 2026 – TU Delft – The Netherlands

Platinum Sponsor

Gold Sponsors

Silver Sponsors

Organisation